Nontrivial flat bands and quantum Hall crossovers in square-octagon lattice materials

Amrita Mukherjee, ¹ Rahul Verma, ¹ Pritesh Srivastava, ¹ and Bahadur Singh^{1,*}

¹ Department of Condensed Matter Physics and Materials Science,

Tata Institute of Fundamental Research, Mumbai 400005, India

Coexistence of nontrivial topology and flat electronic bands in low-energy lattices provides a fertile platform for correlated quantum states. The square-octagon lattice hosts Dirac nodes and flat bands at half-filling, yet the influence of intrinsic spin-orbit coupling (SOC) and staggered magnetic flux on its topological and flat-band properties remains largely unexplored. Here, we examine this lattice using tight-binding models that include SOC and magnetic flux, uncovering a quantum spin Hall phase with spin Chern number $C_s=1$, crossovers to quantum anomalous Hall phases with C=1 and C=2, and higher-order topological insulator phases carrying quantized quadrupolar corner charges. The initially dispersionless flat bands evolve into quasi-flat, topologically nontrivial bands with uniform quantum geometry and large flatness ratios, conducive to fractional Chern insulator states. We further identify realistic material candidates, including octagraphene, transition-metal dichalcogenides, synthetic MoSi₂N₄, and magnetic α -MnO₂, as potential candidates for realizing tunable topological phases intertwined with flat-band physics, opening new opportunities for correlated topological matter.

Introduction. Flat-band materials with coexisting topological states are a cornerstone of condensed matter research. They reveal phases where topology, electronic correlations, and quantum geometry are deeply intertwined [1–5]. Low-energy lattice models hosting Dirac states and flat bands provide natural platforms for correlated topological phases, where spin-orbit coupling or magnetic flux lifts band degeneracies, opens topological gaps, and reshapes the flat-band dispersion. Graphene with a honeycomb lattice is a prime example [6]. It hosts Dirac points at the K valleys that can be gapped to produce quantum spin Hall (QSH) and quantum anomalous Hall (QAH) states [7–9]. However, flat bands in graphene arise only through moiré superlattices, which require precise structural tuning and thus limit broader experimental accessibility [10].

In contrast, Kagome and Lieb lattices naturally generate flat bands through quantum state interference and geometric phase cancellation, avoiding complex structural control[11–13]. Kagome metals such as AV_3Sb_5 (A=K,Rb,Cs) host diverse quantum phases, including nontrivial topology, time-reversal symmetry-breaking states, and superconductivity [14]. Their Ti–Bi analogues, ATi_3Bi_5 [15, 16], preserve kagome electronic features while exhibiting nematic and superconducting states. Lieb lattices, though rare in crystalline form, have been realized in molecular assemblies, photonic systems, cold atoms, and covalent organic frameworks, enabling controlled access to flat and Dirac bands in artificial lattices [17–20].

Square-octagon lattices have recently emerged as another promising two-dimensional geometry where Dirac states coexist with flat bands [21–24]. Theoretical models predict two flat bands—one near half filling and another at the top of the spectrum—alongside van Hove singularities, which are points in the band structure where the density of states diverges. Staggered magnetic flux can

induce nontrivial topology, producing QAH and higherorder topological insulator (HOTI) phases [25, 26]. Material realizations of the square-octagon lattice include carbon allotropes such as octagraphene, transition-metal dichalcogenide monolayers, magnetic compounds including hollandites, and nitride monolayers [27–38]. However, despite these theoretical and experimental advances, it remains unclear how intrinsic SOC and staggered flux influence the topological and flat-band characteristics of the square-octagon lattice. In particular, it is an open question whether these perturbations can generate nontrivial quantum geometry [39–41] capable of supporting correlated phases such as fractional Chern insulators.

Here we show that intrinsic SOC and staggered magnetic flux in the square-octagon lattice drive a series of topological crossovers among QSH, QAH, and HOTI phases. We trace the evolution of the flat bands and demonstrate how they acquire high flatness and nontrivial quantum geometry. Based on first-principles calculations, we identify realistic material candidates-including transition-metal dichalcogenides, MoSi₂N₄ derivatives, and magnetic α -MnO₂-as promising platforms for realizing switchable topological and flat-band phenomena. Our results establish the square-octagon lattice as a robust framework where nontrivial geometry and topology coexist to generate rich quantum states. Model Hamiltonian and band structure. The squareoctagon lattice comprises four sublattices per unit cell, as illustrated in Fig. 1(a). It is characterized by nearestneighbour (NN) intracell hopping t_1 , intercell hopping t_2 , and next-nearest-neighbour (NNN) diagonal hopping λ . For $t_2 = t_1$, the system forms an undimerized, uniform square-octagon network. A staggered magnetic flux applied to each square plaquette introduces an Aharonov-Bohm phase, such that NN hoppings acquire a factor $e^{\pm i\theta}$, where $\theta=\frac{2\pi\Phi}{4\Phi_0}$ and $\Phi_0=\frac{hc}{e}$ is the magnetic flux quantum. The \pm sign denotes the hopping direc-

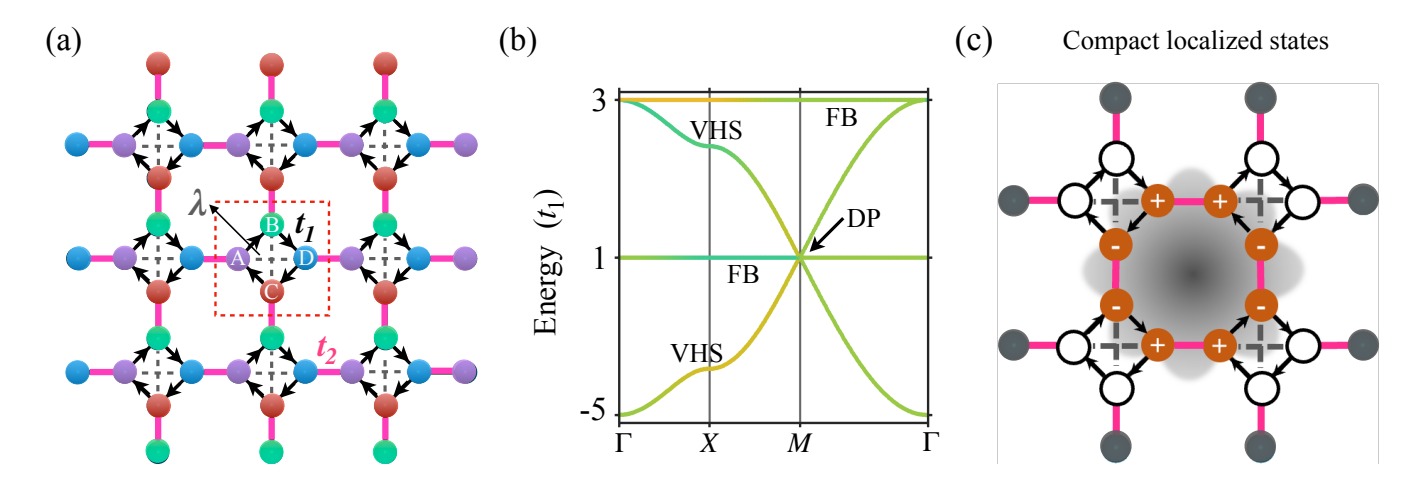


FIG. 1. Coexistence of flat bands and Dirac cones in a square-octagon lattice. (a) Square-octagon lattice with four sublattices (A-D) per unit cell, shown in distinct colors. t_1 , λ , and t_2 represent the nearest-neighbor, next-nearest-neighbor, and intercell hopping parameters, respectively. Arrows indicate the magnetic flux directions. (b) Energy dispersion for $t_2 = 2t_1$ and $\lambda = t_1$. Van Hove singularities (VHSs), flat bands (FBs), and a Dirac point (DP) are marked. Colors denote the dominant sublattice contributions to each band. (c) Schematic of a compact localized state associated with the FB at $E = t_1$ (gray). Filled and hollow sites correspond to nonzero and zero wavefunction amplitudes, respectively. The \pm signs indicate phase alternation leading to destructive interference at the hollow sites, which localizes the state.

tion along the square loop, as indicated by the arrows in Fig. 1(a).

In presence of flux and intrinsic SOC, the system is described by a single-orbital tight-binding Hamiltonian,

$$H = H_{\rm NN} + H_{\rm SOC} \tag{1}$$

where $H_{\rm NN}$ and $H_{\rm SOC}$ denote the spin-independent hopping and intrinsic SOC terms, respectively:

$$H_{\rm NN} = -t_1 \sum_{\langle j,k \rangle} e^{i\theta} c_j^{\dagger} c_k - t_2 \sum_{\langle j,k \rangle'} c_j^{\dagger} c_k - \lambda \sum_{\langle \langle j,k \rangle \rangle} c_j^{\dagger} c_k + H.c.,$$
(2)

and

$$H_{\text{SOC}} = i\lambda_{\text{SOC}} \sum_{\langle \langle j, k \rangle \rangle, \sigma \sigma'} c_{j\sigma}^{\dagger} (\mathbf{e}_{jk} \cdot \boldsymbol{\sigma}) c_{k\sigma}$$
 (3)

Here, $\hat{c}_{j\sigma}^{\dagger}$ ($\hat{c}_{j\sigma}$) is the creation (annihilation) operator for an electron at site j with spin σ . σ are the Pauli matrices, and $\lambda_{\rm SOC}$ is the intrinsic SOC strength. Here, $\lambda_{\rm SOC}$ is expressed in unit of t_1 . The factor $\mathbf{e}_{jk} = (\mathbf{d}_{jk}^1 \times \mathbf{d}_{jk}^2)_z = \pm 1$ encodes the direction of hopping between two NNN sites j and k, defined by unit vectors \mathbf{d}_{jk}^1 and \mathbf{d}_{jk}^2 along the corresponding bonds [3, 7]. Under periodic boundary conditions, the Hamiltonian becomes

$$H = \sum_{\mathbf{k}} \psi_{\mathbf{k}}^{\dagger} \hat{\mathcal{H}}(\mathbf{k}) \psi_{\mathbf{k}} \tag{4}$$

with spinor basis $\psi_{\boldsymbol{k}}^{\dagger} = (\psi_{\boldsymbol{k}\uparrow}^{\dagger}, \psi_{\boldsymbol{k}\downarrow}^{\dagger})$, where $\psi_{\boldsymbol{k}\sigma}^{\dagger} = (c_{A\boldsymbol{k}\sigma}^{\dagger}, c_{B\boldsymbol{k}\sigma}^{\dagger}, c_{C\boldsymbol{k}\sigma}^{\dagger}, c_{D\boldsymbol{k}\sigma}^{\dagger})$. $\hat{\mathcal{H}}(\boldsymbol{k})$ represents the momentum-space Hamiltonian.

For $\lambda = t_1$ and in the absence of SOC and magnetic flux, the eigenvalues of $\hat{\mathcal{H}}(\mathbf{k})$ are

$$\begin{cases}
E_{n=1-4} = t_1 \pm t_2, \\
-t_1 \pm \sqrt{4t_1^2 + t_2^2 + 2t_1t_2(\cos k_x + \cos k_y)}
\end{cases} (5)$$

The corresponding band structure for $t_2=2t_1$ and $\lambda=t_1$, with sublattice projections in the square Brillouin zone, is shown in Fig. 1(b). The spectrum hosts two flat bands, one near half-filling and another at the top of the manifold. These flat bands touch dispersive bands at the M point (half-filling) and the Γ point (3/4 filling), forming symmetry-protected Dirac crossings. Their energy positions shift with t_2 , but their nondispersive character persists.

The real-space localization of these flat bands is revealed by solving the Schrödinger equation $H\psi_i = E\psi_i$, where ψ_i is the wavefunction at site i [42]. For the flat band at E = 0 [Fig. 1(b)], the eigenstate exhibits complete localization over a finite cluster, with nonzero amplitudes confined within the cluster (brown sites) and vanishing amplitudes outside it (white sites), as illustrated in Fig. 1(c). This compact localized state (CLS), analogous to those in Lieb and kagome lattices, underlies the nondispersive nature of the flat bands and their topological origin.

Topological state crossovers. The evolution of the square-octagon band structure with intrinsic SOC and magnetic flux Φ is shown in Fig. 2. A finite SOC strength ($|\lambda_{\rm SOC}| > 0$) gaps the Dirac crossings, producing inverted band gaps at the M point (half-filling) and the Γ point (3/4 filling), as shown in Fig. 2(a) for $\lambda_{\rm SOC} = 0.1$. Parity analysis yields $\mathbb{Z}_2 = 1$, confirming a topological insulat-

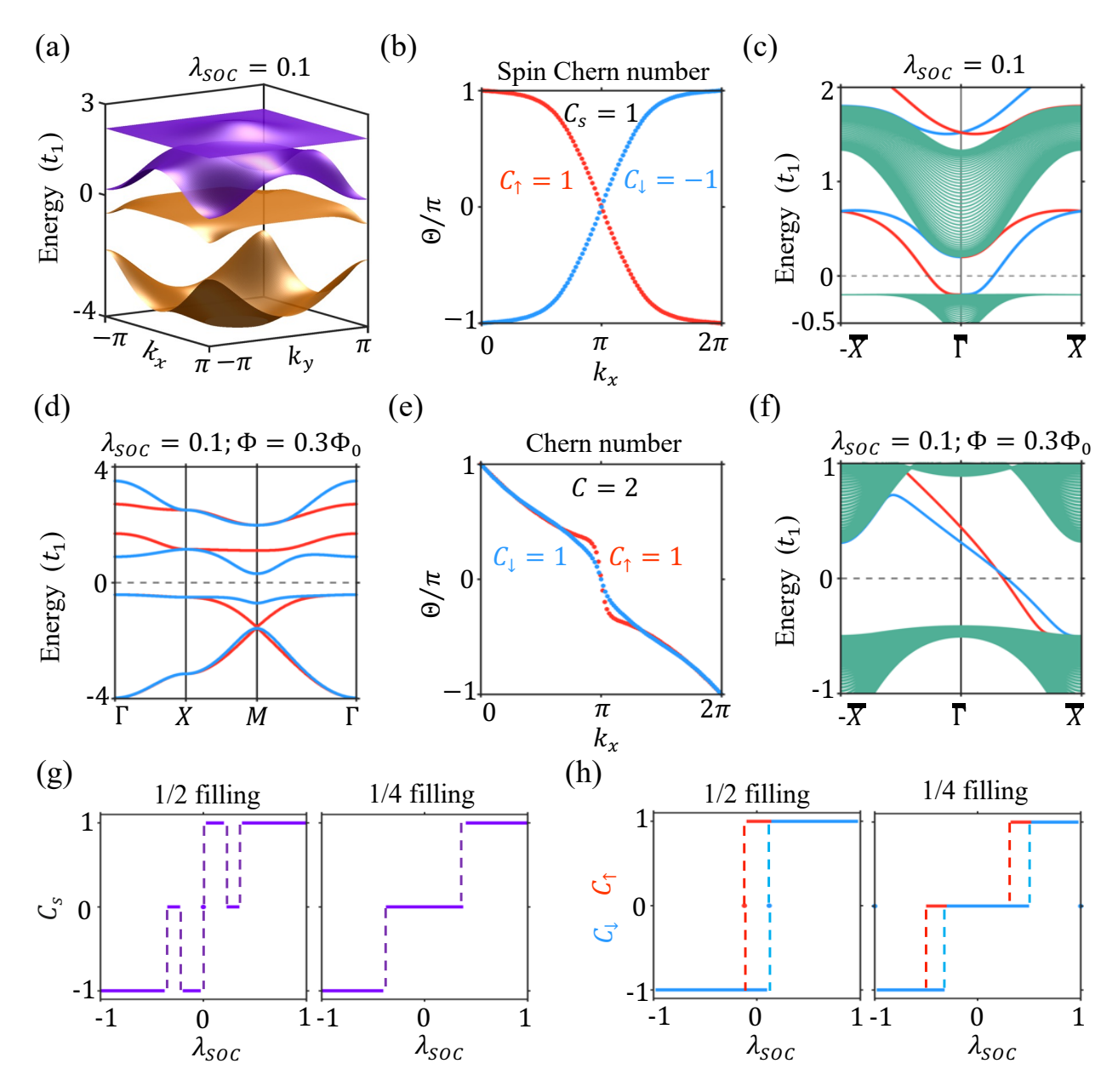


FIG. 2. Emergence of quantum Hall phases and nontrivial flat bands in square-octagonal lattice. (a) Band structure with SOC strength $\lambda_{SOC}=0.1$ and intercell hopping $t_2=1.2t_1$. A nontrivial band gap opens across the full Brillouin zone (BZ) at half-filling, giving rise to a quantum spin Hall phase. Occupied and unoccupied bands are shown in orange and violet, respectively. (b) Evolution of Wannier charge centers for two spin channels, exhibiting zero total Chern number but a finite spin Chern number. (c) Edge-state spectrum along the (010) direction, showing spin-polarized edge modes. (d) Band structure in the presence of SOC ($\lambda_{SOC}=0.1$) and magnetic flux $\Phi=0.3\Phi_0$. (e) Corresponding WCC evolution for two spin channels and (f) associated chiral edge states, indicating a quantum anomalous Hall phase with Chern number C=2 (QAH II). (g) Evolution of the spin Chern number with SOC strength λ_{SOC} at 1/2 and 1/4 fillings. (h) Evolution of Chern number as a function of magnetic flux Φ at the same fillings.

ing phase. This is further supported by the spin-resolved Wannier charge center (WCC) spectrum in Fig. 2(b). The associated spin Chern number, obtained from the WCC flow, is $C_s = \frac{1}{2}(C_{\uparrow} - C_{\downarrow}) = 1$. Here, C_{\uparrow} and C_{\downarrow} denote the Chern numbers of the up- and down-spin channels, respectively. These are evaluated from the band-

resolved Chern number,

$$C_n = \frac{1}{2\pi} \int_{BZ} d^2 \mathbf{k} \ \Omega_{n,xy}(\mathbf{k}), \tag{6}$$

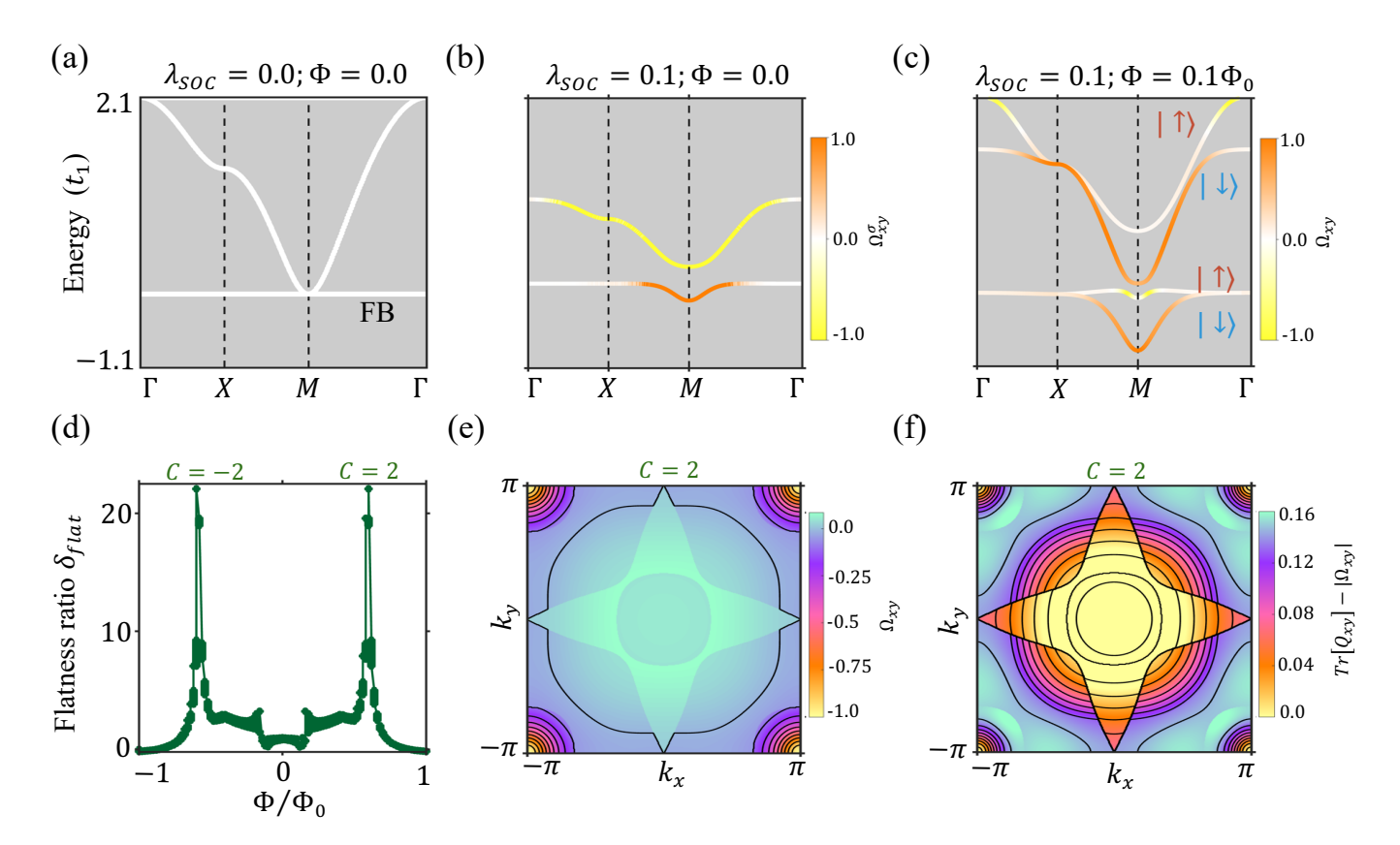


FIG. 3. Nontrivial flatness and quantum geometry. (a-c) Evolution of the flat band and Dirac cone at the M point: (a) without SOC, (b) with SOC, and (c) with both SOC and magnetic flux. The gapless Dirac point in the absence of SOC evolves into a QSH phase with SOC and a QAH phase under magnetic flux. Color maps indicate (b) the spin Berry curvature Ω_{xy}^{σ} and (c) the Berry curvature Ω_{xy} associated with band inversion. Flat bands acquire finite dispersion near the inversion point, forming quasi-flat topological bands. (d) Flatness ratio of flat band (at half-filling) as a function of magnetic flux Φ for $t_2 = 1.2t_1$ and $\lambda_{SOC} = 0.1$. Green regions denote the QAH phase with $C = \pm 2$, where the topological flat band retains a high flatness ratio. (e,f) Contour maps of (e) Berry curvature Ω_{xy} and (f) the difference between the trace of the quantum metric and the absolute value of Berry curvature, $\text{Tr}[Q_{xy}] - |\Omega_{xy}|$, for the topological band with flatness ratio ~ 22 and Chern numbers C = 2 and C = -2.

with the Berry curvature [43]

$$\Omega_{n,xy}(\mathbf{k}) = \hbar^2 \sum_{E_m \neq E_n} -2 \operatorname{Im} \frac{\langle \psi_n(\mathbf{k}) | v_x | \psi_m(\mathbf{k}) \rangle \langle \psi_m(\mathbf{k}) | v_y | \psi_n(\mathbf{k}) \rangle}{(E_n - E_m)^2}$$

where $|\psi_n(\mathbf{k})\rangle$ is the n^{th} Bloch state, and $v_x =$ $\partial \hat{\mathcal{H}}(\mathbf{k})/\partial k_x$, $v_y = \partial \hat{\mathcal{H}}(\mathbf{k})/\partial k_y$ are velocity operators. From WCC analysis, $C_{\uparrow} = 1$ and $C_{\downarrow} = -1$, giving a total Chern number C=0 (consistent with time-reversal symmetry) but a finite spin Chern number $C_s = 1$, characteristic of the QSH phase.

The edge spectrum in Fig. 2(c) exhibits helical counterpropagating edge modes within the bulk gap, consistent with $\mathbb{Z}_2 = 1$ and $C_s = 1$. These helical states appear at both half- and 3/4 filling, forming a ladder-like sequence of edge channels. As λ_{SOC} increases, the nontrivial gaps and edge states remain robust, while the flat bands evolve into quasi-flat bands. The evolution of C_s with λ_{SOC} at half- and quarter-filling, shown in Fig. 2(g), follows a staircase trend: $C_s = 1$ at small λ_{SOC} , vanishing at a crit-

ical $\lambda_{SOC} = 0.225$ due to band inversion, and reemerging as $C_s = 1$ for $\lambda_{SOC} > 0.35$. Reversing the sign of λ_{SOC} $\Omega_{n,xy}(\mathbf{k}) = \hbar^2 \sum_{E_m \neq E_n} -2 \operatorname{Im} \frac{\langle \psi_n(\mathbf{k}) | v_x | \psi_m(\mathbf{k}) \rangle \langle \psi_m(\mathbf{k}) | v_y | \psi_n(\mathbf{k}) \rangle}{(E_n - E_m)^2}, \text{ yields } C_s = -1, \text{ reversing the edge-state chirality, analogous to the positive-negative SOC interplay observed in$ HgTe and HgSe [44]. This tunability demonstrates that the QSH phase can be switched by locking or unlocking band inversions through SOC strength.

> Introducing a magnetic flux Φ breaks time-reversal symmetry, lifts Kramers degeneracy, and separates the spin channels, driving a crossover from the QSH to the QAH regime. For $\lambda_{SOC} = 0.1$ and $\Phi = 0.3\Phi_0$, the band structure in Fig. 2(d) shows lifted spin degeneracy, with unidirectional WCC flows for both spin channels (Fig. 2(e)), resulting in a total Chern number C=2. The corresponding edge spectrum in Fig. 2(f) reveals two chiral edge states propagating in the same direction, defining a QAH-II phase (C = 2). With increasing Φ , the inverted gap in one spin channel closes while widening in the other, leading to a QAH-I phase with C=1. The evolution of spin-resolved Chern numbers with Φ

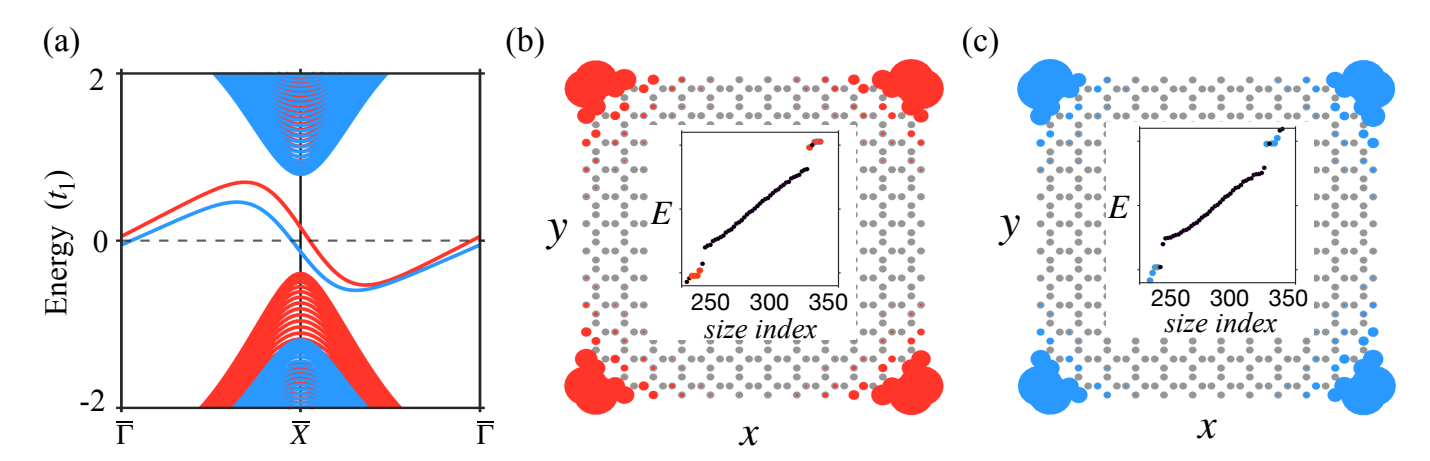


FIG. 4. Higher-order topological insulator with quadrupolar charge. (a) Edge band structure for magnetic flux $\Phi = 0.5\Phi_0$, intercell hopping integral $t_2 = 3.2t_1$ and spin-orbit coupling $\lambda_{\rm SOC} = 0.1$, showing spin-polarized floating edge states. (b,c) Spatial distribution of corner-state wavefunctions $|\psi|^2$ at $E = t_1$ for up (red) and down (blue) spin channels. Fourfold-degenerate spin-polarized corner states appear at $E = \pm t_1$. Insets display the energy spectrum, highlighting red and blue states within the nontrivial bulk gap.

(Fig. 2(h)) shows that the QAH-II phase persists over a wide flux range at half-filling, while spin-selective QAH-I phases ($C=\pm 1$) appear at quarter-filling. These results establish that both SOC and magnetic flux serve as effective tuning knobs for engineering topological crossovers in the square-octagon lattice.

Emergence of nontrivial flat bands. We next examine how the flat bands evolve and acquire nontrivial topology under the combined effects of SOC (λ_{SOC}) and magnetic flux (Φ) . When both λ_{SOC} and Φ are present, the perfectly flat band transforms into a quasi-flat band with a small dispersion near the M point (Figs. 3(a-c)). SOC induces finite spin-Berry curvature, while the magnetic flux breaks time-reversal symmetry and generates spin-dependent topological flat bands with nonzero Berry curvature. The flatness ratio, defined as $\delta_{\rm flat} = \Delta_q/\mathcal{W}$ (where Δ_q is the band gap and \mathcal{W} the bandwidth) [4, 5], quantifies the propensity of a band to host interactiondriven topological phases. Its dependence on Φ and the intercell hopping t_2 for both spin channels is shown in Fig. 3(d), along with the corresponding Chern numbers. Sharp peaks appear in narrow parameter ranges, with $\delta_{\rm flat}$ reaching values up to ~ 22 in the $C=\pm 2$ phase at half-filling for $t_2 = 1.2t_1$ and $\Phi = 0.6\Phi_0$.

To assess the potential for fractional Chern insulators (FCIs), we further analyze the band geometry using the quantum geometric tensor [39–41],

$$g_{n,xy}(\mathbf{k}) = \sum_{E_m \neq E_n} \frac{\langle \psi_n(\mathbf{k}) | \frac{\partial \hat{\mathcal{H}}(\mathbf{k})}{\partial k_x} | \psi_m(\mathbf{k}) \rangle \langle \psi_m(\mathbf{k}) | \frac{\partial \hat{\mathcal{H}}(\mathbf{k})}{\partial k_y} | \psi_n(\mathbf{k}) \rangle}{(E_n - E_m)^2},$$

where $|\psi_n(\mathbf{k})\rangle$ is the *n*th Bloch state. The real and imaginary parts of $g_{n,xy}$ yield the quantum metric and Berry curvature, respectively: $Q_{xy} = \text{Re}[g_{n,xy}]$ and $\Omega_{xy} = -2\text{Im}[g_{n,xy}]$. The stability criterion for FCIs, $\text{Tr}[Q_{xy}] - |\Omega_{xy}|$, quantifies the uniformity of the band

geometry and topology across the Brillouin zone. In regions of high flatness, this difference remains nearly uniform (small but finite), indicating geometric conditions favorable for stabilizing FCIs. Two distinct regimes of enhanced flatness with $C=\pm 2$ are identified (Fig. 3(d)). Figures 3(e,f) present the Berry curvature Ω_{xy} and the corresponding ${\rm Tr}[Q_{xy}]-|\Omega_{xy}|$ distribution for the topological flat band with the optimal flatness ratio, confirming that the Chern band satisfies the geometric inequality dictated by the Fubini–Study metric [39–41]. These results demonstrate that the square–octagon lattice, when tuned by SOC, magnetic flux, and hopping parameters, provides a robust platform with favorable band geometry for fractional topological phases.

Higher-order topological state and phase diagram. Building on the discussion of QSH and QAH phases, we now examine how intercell hopping t_2 drives further topological transitions. For fixed $\lambda_{\rm SOC}=0.1t_1$ and $\Phi=0.3\Phi_0$, increasing t_2 initially stabilizes a QAH I phase in the spin-up channel, characterized by a chiral edge state with C=1. As t_2 increases, a subsequent inversion in the spin-down channel generates floating edge bands (FEBs) detached from the bulk continuum, while the spin-up channel retains C=1. Upon further tuning t_2 , both spin channels evolve into a HOTI with C=0, where the FEBs remain isolated from the bulk, as shown in Fig. 4(a) for $t_2=3.2t_1$ and $\Phi=0.5\Phi_0$.

Although the total Chern number vanishes, the HOTI phase exhibits a quantized quadrupole moment $Q_{xy} = 1/2$. This quadrupolar moment is computed from the bulk polarization [45],

$$P_{x/y}^{\sigma} = -\frac{i}{2\pi} \log \left[\det \left(\nu_{k_{x/y} + 2\pi \leftarrow k_{x/y}}^{\sigma} \right) \right], \tag{9}$$

where ν denotes the Wilson loop spectrum of the occupied bands for spin channel σ . The spin-resolved

and total quadrupole moments are then given by $Q_{ij}^{\sigma} = P_i^{\sigma}P_j^{\sigma}$, $i,j \in x,y$, $Q_{ij} = \sum_{\sigma}Q_{ij}^{\sigma}$. A finite Q_{xy} ensures the presence of corner-localized modes coexisting with gapless FEBs. Figures 4(b,c) display the energy spectrum of a nanodisk, where corner states for both spin channels appear within the bulk-edge gaps at discrete energies $E = \pm t_1$, exhibiting strong localization at the corners. This confirms that the HOTI phase in the square–octagon lattice hosts a robust quadrupolar corner charge, providing a platform where first- and higher-order topological phases coexist.

The complete topological phase diagram as a function of t_2 and Φ is shown in Fig. 5(a). It reveals how the interplay between flux, SOC, and intercell hopping governs successive band inversions in the spin-resolved channels. For small t_2 and zero flux, SOC opens a nontrivial gap, realizing a QSH state with helical edge modes protected by time-reversal symmetry. Increasing Φ drives the system into the QAH I phase $(C = \pm 1)$ with a single-spin inversion, and subsequently into QAH II (C = 2) with both spin band inversion that contribute co-propagating chiral edge states. At intermediate t_2 , a second inversion in one spin channel gives rise to the QAH I' phase (C = 1)and generates a detached spin-polarized FEBs. Beyond a critical t_2 , both spin channels undergo further inversion, stabilizing a HOTI phase (C = 0) with spin-degenerate corner states and FEBs. Specifically, for $t_2 \in [2.2, 2.6]$, one spin channel remains in the QAH state while the other develops FEBs, marking the transition region toward HOTI behavior. Such FEBs, rarely reported in prior studies, can serve as distinct hallmarks of higherorder topology in the square-octagon lattice. Moreover, the topological flat bands evolve into quasi-flat bands with enhanced flatness ratios, as shown in Fig. 5(b). Figures 5(c-h) schematically summarize the corresponding band structures across these topological regimes.

Materials realization. We explored possible material platforms hosting the square-octagonal lattice geometry. This lattice appears across several material classes, including carbon allotropes, group-Va elements, transition-metal dichalcogenides (TMDs), nitrides, phosphides, carbides such as GaN and AlN, the synthetic $MoSi_2N_4$ family, and magnetic compounds including MnN and hollandites [27–38]. Here, we focus on a few representative examples, shown in Fig. 6, which illustrate the diversity of tunable electronic and topological phases in nonmagnetic systems.

First-principles calculations were performed within the density functional theory (DFT) framework using projector augmented-wave (PAW) potentials as implemented in the Vienna *ab initio* simulation package (VASP) [46, 47]. Exchange-correlation effects were treated using the generalized gradient approximation (GGA), and SOC was included self-consistently to account for relativistic effects [48]. Material-specific tight-binding Hamiltonians were constructed via the VASP2WANNIER90 inter-

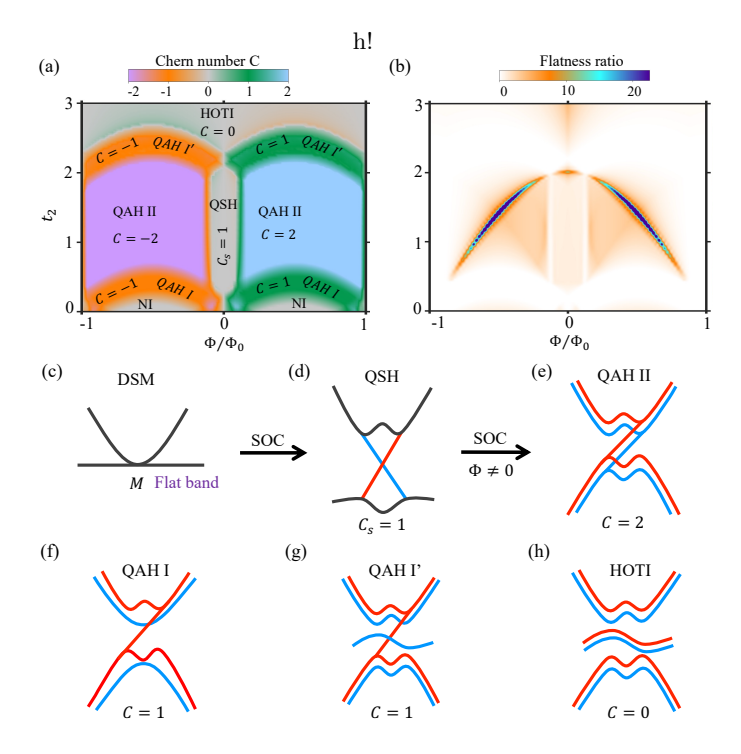


FIG. 5. Topological phase diagram and spin-polarized topological flat bands. (a) Phase diagram with intercell hopping t_2 (vertical axis) and magnetic flux Φ (horizontal axis). The intrinsic SOC strength is fixed at $\lambda_{SOC}=0.1$ with $\lambda=t_1$ and $t_1=1$. Distinct phases are identified by their Chern number C or spin Chern number C_s : quantum anomalous Hall (QAH, QAH I, QAH I', QAH II), quantum spin Hall (QSH), higher-order topological insulator (HOTI), and normal insulator (NI). (b) Flatness ratio as a function of t_2 and Φ at half filling. (c-h) Representative band structures of the corresponding phases and the evolution of flat bands in the square-octagon lattice under SOC and magnetic flux. Red and blue denote spin-up and spin-down projections, while black lines represent spin-degenerate bands.

face [49], and edge states were obtained using the semi-infinite Green's function method [50].

Figure 6(a) shows the crystal structure of octagraphene (T-graphene), where carbon atoms form a square-octagonal lattice with unequal sp^2 hybridization arising from distinct inter- and intra-square C-C bond lengths. The orbital-resolved band structure (Fig. 6(d)) reveals metallic behavior, with states near the Fermi level dominated by carbon p_z orbitals (blue). The dispersion exhibits electron and hole pockets at the Γ and M points, respectively, along with quasi-flat bands along $\Gamma - X$ and M - X directions.

In TMDs, the square-octagonal geometry can form through 4-8 defects at grain boundaries of monolayer MoS_2 [30, 31]. Structurally, MoS_2 consists of three atomic layers, with Mo atoms coordinated by six neighboring S atoms in a square-octagonal network. The calculated electronic dispersion near the Fermi level without SOC (Fig. 6(e)) shows semimetallic behavior, featuring

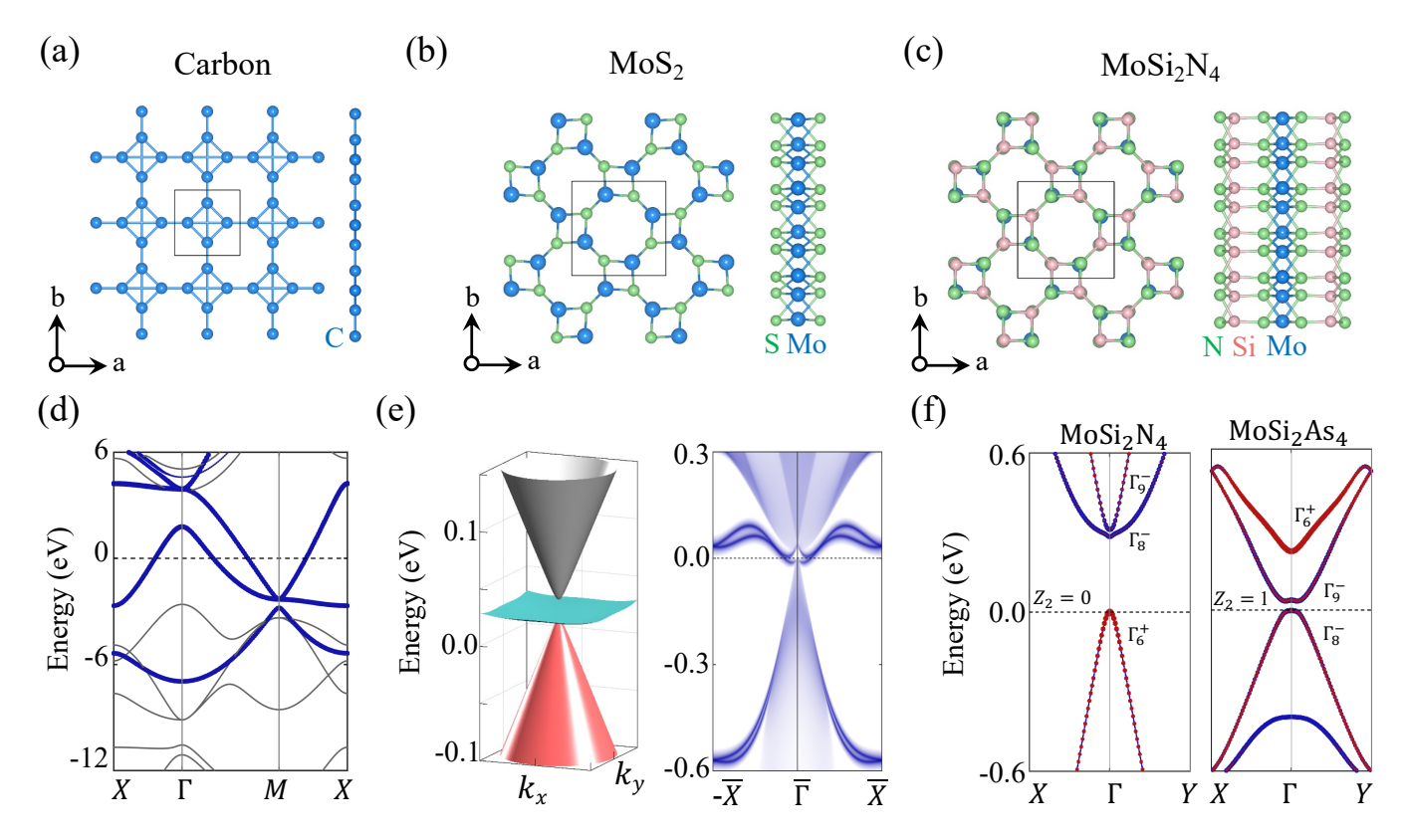


FIG. 6. Materials realizing square—octagonal lattice geometry: Top and side views of square-octagon monolayers of (a) carbon, (b) transition metal dichalcogenide MoS_2 , (c) bottom-up designed synthetic $MoSi_2N_4$. The corresponding electronic band structures are shown for (d) carbon, (e) $MoSi_2$, (f) $MoSi_2N_4$. These systems exhibit diverse quantum phases, including a metallic state in carbon, coexisting Dirac-like bands and a quantum spin Hall state with a van Hove singularity near the Fermi level in $MoSi_2$, a tunable topological state in $MoSi_2N_4$.

Dirac-like bands and a nearly flat band at Γ . The top valence and bottom conduction bands, dominated by Mo d_{z^2} and $d_{x^2-y^2}$ orbitals with opposite parities, are degenerate at the Fermi level. SOC lifts this degeneracy, opening a gap and producing a QSH phase with nontrivial $\mathbb{Z}_2 = 1$ and $C_s = 1$. The corresponding helical edge states are shown in Fig. 6(e). Breaking C_4 symmetry splits the Γ -point Dirac node into two Dirac cones, leading to van Hove singularities at Γ [31]. Strain further drives topological phase transitions, tuning MoS₂ between QSH, trivial insulating, and metallic phases.

 $MoSi_2N_4$ monolayers Synthetic with square-octagonal framework offer another tunable platform for topological phases and flat bands [35]. The central MoN_2 layer resembles that of TMDs and is sandwiched between two SiN layers, forming a sevenatom-thick structure. Figure 6(f) displays the band structures and irreducible representations near the Fermi level for two representative compositions. In MoSi₂N₄, the valence band maximum at Γ primarily derives from Mo $d_{x^2-y^2}$ orbitals (red), while the conduction band minimum originates from doubly degenerate d_{z^2} orbitals (blue), yielding a topologically trivial direct-gap insulator ($\mathbb{Z}_2 = 0$). Substituting N with As induces

a band inversion at Γ , producing a doubly degenerate state at the Fermi level. SOC then opens a gap, realizing a QSH phase with $\mathbb{Z}_2 = 1$ and $C_s = 1$. Consequently, $\text{MoSi}_2(N_x \text{As}_{1-x})_4$ enables continuous tuning between trivial and topological insulating states via chemical substitutions.

Finally, several magnetic compounds, such as hollandites [37, 38], also crystallize in square-octagonal frameworks and can host spin-polarized topological states. Their double chains of edge-sharing $\rm MnO_6$ octahedra form distorted square-octagon motifs, generating partially flat d_{xy} -derived bands and gapped Dirac crossings at Γ and M (not shown for brevity). The resulting magnetic frustration and anisotropy lead to competing magnetic orders, offering a possible route to spin-liquid-like behavior.

Summary. We have demonstrated a rich landscape of topological phases in a two-dimensional square-octagon lattice that hosts both Dirac states and nontrivial flat bands. This lattice supports two flat bands: one pinned at the apex of the Dirac cone at half-filling and the other capping the overall band dispersion. The inclusion of SOC opens nontrivial energy gaps at the Dirac points, realizing a QSH phase with $C_s = 1$. Introducing a stag-

gered magnetic flux Φ breaks time-reversal symmetry, lifts the Kramers degeneracy, and induces QAH phases with Chern numbers C=1 and C=2. Systematic tuning of the intercell hopping parameter t_2 , which governs lattice dimerization, drives topological crossovers from QAH phases with chiral edge modes to HOTI phases characterized by floating edge bands and a quantized quadrupolar charge. The interplay among SOC, magnetic flux, and t_2 further renders the flat bands quasiflat and topologically nontrivial, with regions of parameter space exhibiting remarkably high flatness ratios of ~ 22 for $C=\pm 2$. These quasi-flat bands possess nearly uniform quantum geometric tensor distributions, establishing favorable conditions for realizing fractional Chern insulator states.

We have also identified realistic material candidates with square—octagonal lattice geometry, such as octagraphene, MoS₂, and MoSi₂(N, As)₄, where Dirac-like and flat-band features dominate the low-energy electronic structure, facilitating diverse topological phases. Unlike in kagome or Lieb lattices, the flat bands in the square-octagon system are intrinsically pinned at the Dirac point at half-filling, making them more robust and conducive to interaction-driven topological phenomena. Our results establish the square—octagon lattice as a versatile and tunable platform for engineering coexisting topological and flat-band phases, opening promising avenues for exploring correlated topological matter and potential applications in next-generation electronic and spintronic devices.

ACKNOWLEDGEMENT

We thank Bikash Patra for helpful discussions. This work is supported by the Department of Atomic Energy of the Government of India under Project No. 12-R&D-TFR-5.10-0100 and benefited from the computational resources of TIFR Mumbai.

- * Contact author: bahadur.singh@tifr.res.in
- K. Sun, Z. Gu, H. Katsura, and S. Das Sarma, Nearly flatbands with nontrivial topology, Phys. Rev. Lett. 106, 236803 (2011).
- [2] W. Jiang, M. Kang, H. Huang, H. Xu, T. Low, and F. Liu, Topological band evolution between Lieb and kagome lattices, Phys. Rev. B 99, 125131 (2019).
- [3] D.-S. Ma, Y. Xu, C. S. Chiu, N. Regnault, A. A. Houck, Z. Song, and B. A. Bernevig, Spin-orbit-induced topological flat bands in line and split graphs of bipartite lattices, Phys. Rev. Lett. 125, 266403 (2020).
- [4] D.-H. Guan, L. Qi, X. Zhang, Y. Liu, and A.-L. He, Staggered magnetic flux induced higher-order topological insulators and topological flat bands on the ruby lattice, Phys. Rev. B 108, 085121 (2023).

- [5] A.-L. He, X.-H. Yan, L. Qi, Y. Liu, and Y. Han, Topological states and flat bands on the maple leaf lattice, Phys. Rev. B 109, 075118 (2024).
- [6] A. K. Geim and K. S. Novoselov, The rise of graphene, Nat. Mater. 6, 183 (2007).
- [7] C. L. Kane and E. J. Mele, Quantum spin Hall effect in graphene, Phys. Rev. Lett. 95, 226801 (2005).
- [8] C. L. Kane and E. J. Mele, Z₂ topological order and the quantum spin Hall effect, Phys. Rev. Lett. 95, 146802 (2005).
- [9] F. D. M. Haldane, Model for a quantum Hall effect without landau levels: Condensed-matter realization of the "parity anomaly", Phys. Rev. Lett. 61, 2015 (1988).
- [10] E. Suárez Morell, J. D. Correa, P. Vargas, M. Pacheco, and Z. Barticevic, Flat bands in slightly twisted bilayer graphene: Tight-binding calculations, Phys. Rev. B 82, 121407 (2010).
- [11] K. Ohgushi, S. Murakami, and N. Nagaosa, Spin anisotropy and quantum Hall effect in the kagomé lattice: Chiral spin state based on a ferromagnet, Phys. Rev. B 62, R6065 (2000).
- [12] E. H. Lieb, Two theorems on the Hubbard model, Phys. Rev. Lett. 62, 1201 (1989).
- [13] D. Leykam, A. Andreanov, and S. Flach, Artificial flat band systems: from lattice models to experiments, Adv. Phys. X 3, 1473052 (2018).
- [14] Y.-P. Lin and R. M. Nandkishore, Complex charge density waves at Van Hove singularity on hexagonal lattices: Haldane-model phase diagram and potential realization in the kagome metals AV₃Sb₅ (A= K, Rb, Cs), Phys. Rev. B 104, 045122 (2021).
- [15] H. Yang, Y. Ye, Z. Zhao, J. Liu, X.-W. Yi, Y. Zhang, H. Xiao, J. Shi, J.-Y. You, Z. Huang, et al., Superconductivity and nematic order in a new titanium-based kagome metal CsTi₃Bi₅ without charge density wave order, Nat. Commun. 15, 9626 (2024).
- [16] B. Patra, A. Mukherjee, and B. Singh, High-order van Hove singularities and nematic instability in the kagome superconductor CsTi₃Bi₅, Phys. Rev. B 111, 045135 (2025).
- [17] M. R. Slot, T. S. Gardenier, P. H. Jacobse, G. C. Van Miert, S. N. Kempkes, S. J. Zevenhuizen, C. M. Smith, D. Vanmaekelbergh, and I. Swart, Experimental realization and characterization of an electronic Lieb lattice, Nat. Phys. 13, 672 (2017).
- [18] S. Mukherjee, A. Spracklen, D. Choudhury, N. Goldman, P. Öhberg, E. Andersson, and R. R. Thomson, Observation of a localized flat-band state in a photonic Lieb lattice, Phys. Rev. Lett. 114, 245504 (2015).
- [19] S. Taie, H. Ozawa, T. Ichinose, T. Nishio, S. Nakajima, and Y. Takahashi, Coherent driving and freezing of bosonic matter wave in an optical Lieb lattice, Sci. Adv. 1, e1500854 (2015).
- [20] B. Cui, X. Zheng, J. Wang, D. Liu, S. Xie, and B. Huang, Realization of Lieb lattice in covalent-organic frameworks with tunable topology and magnetism, Nat. Commun. 11, 66 (2020).
- [21] M. Kargarian and G. A. Fiete, Topological phases and phase transitions on the square-octagon lattice, Phys. Rev. B 82, 085106 (2010).
- [22] X.-P. Liu, W.-C. Chen, Y.-F. Wang, and C.-D. Gong, Topological quantum phase transitions on the kagomé and square–octagon lattices, J. Phys.: Condens. Matter

- **25**, 305602 (2013).
- [23] L. H. Nunes and C. M. Smith, Flat-band superconductivity for tight-binding electrons on a square-octagon lattice, Phys. Rev. B 101, 224514 (2020).
- [24] P. Wunderlich, F. Ferrari, and R. Valentí, Detecting topological phases in the square–octagon lattice with statistical methods, Euro. Phys. J. Plus 138, 336 (2023).
- [25] B. Pal, Nontrivial topological flat bands in a diamondoctagon lattice geometry, Phys. Rev. B 98, 245116 (2018).
- [26] A.-L. He, W.-W. Luo, Y. Zhou, Y.-F. Wang, and H. Yao, Topological states in a dimerized system with staggered magnetic fluxes, Phys. Rev. B 105, 235139 (2022).
- [27] X.-L. Sheng, H.-J. Cui, F. Ye, Q.-B. Yan, Q.-R. Zheng, and G. Su, Octagraphene as a versatile carbon atomic sheet for novel nanotubes, unconventional fullerenes, and hydrogen storage, J. Appl. Phys. 112, 074315 (2012).
- [28] Y. Liu, G. Wang, Q. Huang, L. Guo, and X. Chen, Structural and electronic properties of T graphene: a two-dimensional carbon allotrope with tetrarings, Phys. Rev. Lett. 108, 225505 (2012).
- [29] T. Gorkan, E. Aktürk, and S. Ciraci, Deformed octagon-hexagon-square structure of group-IV and group-V elements and III-V compounds, Phys. Rev. B 100, 125306 (2019).
- [30] A. M. Van Der Zande, P. Y. Huang, D. A. Chenet, T. C. Berkelbach, Y. You, G.-H. Lee, T. F. Heinz, D. R. Reichman, D. A. Muller, and J. C. Hone, Grains and grain boundaries in highly crystalline monolayer molybdenum disulphide, Nat. Mater. 12, 554 (2013).
- [31] Y. Sun, C. Felser, and B. Yan, Graphene-like Dirac states and quantum spin Hall insulators in square-octagonal MX₂ (M= Mo, W; X= S, Se, Te) isomers, Phys. Rev. B 92, 165421 (2015).
- [32] Y. Zhang, J. Lee, W.-L. Wang, and D.-X. Yao, Twodimensional octagon-structure monolayer of nitrogen group elements and the related nano-structures, Comp. Mater. Sci. 110, 109 (2015).
- [33] G. Barik and S. Pal, Haeckelite phosphorus: an emerging 2D allotrope of phosphorus for potential use in LIBs/SIBs, Phys. Chem. Chem. Phys. 23, 26547 (2021).
- [34] E. Gürbüz, S. Cahangirov, E. Durgun, and S. Ciraci, Single layers and multilayers of GaN and AlN in squareoctagon structure: Stability, electronic properties, and functionalization, Phys. Rev. B 96, 205427 (2017).
- [35] R. Verma, Y. Vardhan, H. Lin, and B. Singh, Emergent spin Hall quantization and high-order van Hove singularities in square-octagonal MA_2Z_4 , arXiv:2510.12935

- (2025).
- [36] X. Lin, Z. Mao, S. Dong, X. Jian, R. Han, and P. Wu, Ferromagnetism and intrinsic half-metallicity of two-dimensional MnN monolayer with square—octagonal structure, J. Phys.: Condens. Matter 33, 225804 (2021).
- [37] Y. Crespo, A. Andreanov, and N. Seriani, Competing antiferromagnetic and spin-glass phases in a hollandite structure, Phys. Rev. B 88, 014202 (2013).
- [38] Y. Crespo and N. Seriani, Electronic and magnetic properties of α -MnO₂ from ab initio calculations, Phys. Rev. B 88, 144428 (2013).
- [39] R. Roy, Band geometry of fractional topological insulators, Phys. Rev. B 90, 165139 (2014).
- [40] T. Ozawa and B. Mera, Relations between topology and the quantum metric for Chern insulators, Phys. Rev. B 104, 045103 (2021).
- [41] A. Kruchkov, Quantum geometry, flat Chern bands, and Wannier orbital quantization, Phys. Rev. B 105, L241102 (2022).
- [42] W. Maimaiti, A. Andreanov, H. C. Park, O. Gendelman, and S. Flach, Compact localized states and flat-band generators in one dimension, Phys. Rev. B 95, 115135 (2017).
- [43] D. Xiao, M.-C. Chang, and Q. Niu, Berry phase effects on electronic properties, Rev. Mod. Phys. 82, 1959 (2010).
- [44] Q.-Z. Wang, S.-C. Wu, C. Felser, B. Yan, and C.-X. Liu, Spin texture and mirror Chern number in Hg-based chalcogenides, Phys. Rev. B 91, 165435 (2015).
- [45] W. A. Benalcazar, B. A. Bernevig, and T. L. Hughes, Quantized electric multipole insulators, Science 357, 61 (2017).
- [46] P. Hohenberg and W. Kohn, Inhomogeneous electron gas, Phys. Rev. 136, B864 (1964).
- [47] G. Kresse and J. Furthmüller, Efficient iterative schemes for ab initio total-energy calculations using a plane-wave basis set, Phys. Rev. B 54, 11169 (1996).
- [48] J. P. Perdew, K. Burke, and M. Ernzerhof, Generalized gradient approximation made simple, Phys. Rev. Lett. 77, 3865 (1996).
- [49] A. A. Mostofi, J. R. Yates, Y.-S. Lee, I. Souza, D. Vanderbilt, and N. Marzari, wannier90: A tool for obtaining maximally-localised Wannier functions, Comput. Phys. Commun. 178, 685 (2008).
- [50] M. L. Sancho, J. L. Sancho, J. L. Sancho, and J. Rubio, Highly convergent schemes for the calculation of bulk and surface Green functions, J. Phys. F: Met. Phys. 15, 851 (1985).